The Astrophysical Journal Letters, 988:L55 (8pp), 2025 August 1 https://doi.org/10.3847/2041-8213/adf185

Atmospheric C/O Ratios of Sub-Neptunes with Magma Oceans: Homemade rather than Inherited

Aaron Werlen[1], Caroline Dorn[1], Hilke E. Schlichting[2], Simon L. Grimm[1,3], and Edward D. Young[2]
[1] Institute for Particle Physics and Astrophysics, ETH Zurich, CH-8093 Zurich, Switzerland; awerlen@ethz.ch
[2] Department of Earth, Planetary, and Space Sciences, University of California, Los Angeles, CA 90095, USA
[3] Department of Astrophysics, University of Zurich, CH-8057 Zurich, Switzerland
Received 2025 April 28; revised 2025 July 16; accepted 2025 July 17; published 2025 July 28

Abstract

Recently, the James Webb Space Telescope has enabled detailed spectroscopic characterization of sub-Neptune atmospheres. With detections of carbon- and oxygen-bearing species such as CO, CO_2, CH_4, and H_2O, a central question is whether the atmospheric C/O ratio, commonly used to trace formation location in giant planets, can serve a similar diagnostic role for sub-Neptunes. We use the global chemical equilibrium framework of H. E. Schlichting & E. D. Young to quantify how magma ocean–atmosphere interactions affect the atmospheric C/O ratio. We find that the resulting C/O ratios range from several orders of magnitude below solar to a few times solar. The atmospheric C/O ratio in sub-Neptunes is therefore not inherited from the protoplanetary disk, but instead emerges from chemical equilibrium between the atmosphere and the underlying magma ocean. Planetary mass, atmospheric mass fraction, and thermal state all strongly influence the atmospheric C/O ratio. In addition, carbon partitioning into the metal phase typically reduces the atmospheric C/O ratio substantially, particularly for atmospheric mass fractions less than a few percent. Finally, we couple the deep equilibrium compositions to 1D atmospheric models that self-consistently solve for the pressure–temperature structure and chemical composition, including photochemistry. We find that the C/O ratio varies with altitude under low vertical mixing conditions ($K_{zz} = 10^4\,\mathrm{cm^2\,s^{-1}}$) but remains constant under strong mixing ($K_{zz} = 10^7\,\mathrm{cm^2\,s^{-1}}$). Our results imply that observed C/O ratios of sub-Neptunes can be used to probe their interiors. Specifically, C/O ratios much lower than host star values would imply an underlying magma ocean with iron metal having sequestered significant amounts of carbon.

Unified Astronomy Thesaurus concepts: Exoplanet atmospheric composition (2021); Exoplanet atmospheric structure (2310); Exoplanet structure (495)

1. Introduction

Efforts to connect atmospheric compositions with planet formation began with retrieval studies of hot Jupiters. N. Madhusudhan et al. (2011) conducted one of the first such studies, inferring a superstellar atmospheric C/O ratio (>1) for WASP-12b based on Spitzer eclipse photometry. However, this result was contested by subsequent analyses, which did not confirm the high C/O ratio (I. J. M. Crossfield et al. 2012; M. Swain et al. 2013; M. R. Line et al. 2014; L. Kreidberg et al. 2015).

In parallel, theoretical studies explored how disk chemistry might influence planetary composition. K. I. Öberg et al. (2011) proposed that the C/O ratio of a planet's atmosphere could be inherited from its formation location relative to the protoplanetary disk's volatile ice lines. In this model, C/O ~ 1 is possible only for planets enriched mainly through gas accretion and formed between the CO and CO_2 ice lines. C. Helling et al. (2014) reached a similar conclusion by modeling the chemical evolution of gas and ices in protoplanetary disks, although they did not simulate planet formation directly.

Later studies incorporated more physically consistent models of planet formation and chemistry. A. Thiabaud et al. (2014, 2015) and U. Marboeuf et al. (2014a, 2014b) modeled planet formation via core accretion, tracking both refractory and volatile element condensation to predict final planetary compositions. N. Madhusudhan et al. (2014) explored whether observed atmospheric abundances could constrain formation pathways for hot Jupiters. They found that giant planets forming in the outer disk could have substellar C/O ratios if their enrichment is dominated by gas accretion. If such planets are found at small orbital distances, this would require inward migration after disk dispersal. C. Mordasini et al. (2016) extended these approaches by modeling the chemical enrichment of giant planets through planetesimal accretion, finding that atmospheric compositions are largely determined by the properties of accreted solids—consistent with observations of both solar system and extrasolar planets.

Within the solar system, formation–composition links have long been used to interpret the atmospheric abundances of giant planets such as Jupiter and Saturn (e.g., O. Mousis et al. 2009). More recently, O. Mousis et al. (2025) interpreted JWST observations of Eris and Makemake using primordial compositional models.

Until recently, such compositional studies have focused primarily on giant or dwarf planets. However, JWST now enables detailed atmospheric characterization of sub-Neptunes (e.g., N. Madhusudhan et al. 2023; B. Benneke et al. 2024; M. Holmberg & N. Madhusudhan 2024; L. Felix et al. 2025; S. P. Schmidt et al. 2025). Notably, B. Benneke et al. (2024) and subsequently L. Felix et al. (2025) reported the first measurement of the atmospheric C/O ratio in the 2.2 $R_\oplus$ sub-Neptune TOI-270d, based on transmission spectroscopy.

Given this new observational access to sub-Neptune atmospheres, a key question that arises is whether their compositions are primarily determined by the accretion of ices in the protoplanetary disk—thereby serving as a tracer of formation history—or whether subsequent processes such as magma

ocean–atmosphere interactions dominate the atmospheric composition.

The interior structure and thermal evolution of sub-Neptunes differ fundamentally from those of hot Jupiters and dwarf planets. Planets with a few Earth masses embedded in a gas disk can accrete several weight percent of hydrogen–helium gas (e.g., E. J. Lee & E. Chiang 2015; S. Ginzburg et al. 2016). During formation, the gravitational binding energy released during a planet's assembly is converted into heat. The resulting temperatures, likely limited by the upper threshold for stable H/He envelopes, can exceed 10^4 K in super-Earths and sub-Neptunes (S. Ginzburg et al. 2016).

The massive H/He envelope acts as an insulating layer, significantly reducing surface cooling and delaying the solidification of the magma ocean to gigayear timescales (e.g., E. D. Lopez & J. J. Fortney 2014; S. Ginzburg et al. 2016). Under such conditions, the planetary surface remains molten for extended periods, allowing continuous chemical exchange between the atmosphere and the interior. Several studies (e.g., S. Ginzburg et al. 2016; Y. Chachan & D. J. Stevenson 2018; E. S. Kite et al. 2019; E. S. Kite & L. Schaefer 2021; H. E. Schlichting & E. D. Young 2022; C. Seo et al. 2024; M. Tian & K. Heng 2024) have shown that understanding these atmosphere–interior interactions is essential for interpreting the evolution and atmospheric composition of sub-Neptunes.

In this study, we investigate how chemical equilibrium between sub-Neptune atmospheres and molten interiors may affect the atmospheric C/O ratio, across a range of planetary masses, atmospheric mass fractions, atmosphere–magma ocean interface (AMOI) temperatures, and silicate–metal equilibrium (SME) temperatures. To this end, we employ the global chemical equilibrium framework introduced by H. E. Schlichting & E. D. Young (2022). We extend this framework to allow carbon to partition from the silicate into the metal phase and analyze how this process modifies the resulting atmospheric C/O ratio.

This Letter is structured as follows. In Section 2, we describe the global chemical equilibrium framework, outline the extensions made to include carbon partitioning between the silicate and metal phases, and present the grid of planetary masses, atmospheric mass fractions, AMOI temperatures, and SME temperatures used in the simulations. We also describe the coupling to a 1D atmospheric model. In Section 3, we present the resulting trends in atmospheric C/O ratios, including the effects of carbon partitioning between phases, and examine their dependence on planetary parameters. In Section 4, we compare our findings to previous studies of magma ocean–atmosphere interaction and discuss implications for interpreting C/O ratios measured by JWST. We summarize our key results and conclusions in Section 5.

2. Methods

2.1. Chemical Thermodynamics

We make use of a variant of the global chemical equilibrium code of H. E. Schlichting & E. D. Young (2022). The code solves a set of linearly independent reactions that span the relevant reaction space for magma ocean–atmosphere interactions. Our model includes 19 chemical reactions involving 26 phase components. Reactions occur within each of the three phases—metal, silicate, and gas—as well as between them. The core, in the astrophysical sense, is composed of two phases: metal and silicate.

We use this definition to underscore that the metal and silicate phases do not necessarily need to be separated by a well-defined core–mantle boundary. Experimental studies (N. Hirao et al. 2004; H. Terasaki et al. 2009; S. Tagawa et al. 2021) have found evidence for limitless hydrogen solubility in metallic phases under high-pressure conditions. Ab initio calculations by Y. Li et al. (2020) support these findings theoretically. The chemical equilibrium code used in this study has also yielded large quantities of hydrogen, oxygen, and silicon in the metallic phase (H. E. Schlichting & E. D. Young 2022; E. D. Young et al. 2023, 2024). Together, these results suggest that a metal phase can harbor large amounts of hydrogen, among other light elements like O and Si. The resulting densities of these metals are comparable to that of the silicate, potentially precluding separation by gravitational settling (E. D. Young et al. 2024).

For this study, we adopt all 18 reactions from H. E. Schlichting & E. D. Young (2022) and expand the network by introducing carbon partitioning from the metal to the silicate phase through the following reaction:

$$\mathrm{C_{metal}} + \mathrm{O_{metal}} \rightleftharpoons \mathrm{CO_{silicate}}. \tag{1}$$

Reaction (1), combined with the reaction set in H. E. Schlichting & E. D. Young (2022), defines an example basis set. All linear combinations of this basis set are, by definition, included in the equilibrium reaction network. For example, although the dissolution of CH_4 is not explicitly listed, it is captured through a combination of reactions involving CH_4 oxidation, CO dissolution, and subsequent carbon partitioning into the metal phase. This means that any pathway involving CH_4 is accounted for in the basis set of reactions and is therefore inherently included in the equilibrium calculation.

Chemical equilibrium for the 19 reactions is obtained by solving the following equilibrium condition for all molar mass fractions x_i:

$$\sum_i \nu_i \ln x_i + \left[\frac{\Delta \hat{G}^\circ_{\mathrm{rxn}}}{RT} + \sum_g \nu_g \ln(P/P^\circ) \right] = 0, \tag{2}$$

where x_i is the mole fraction of species i in its host phase, ν_i are the stoichiometric coefficients for species i, $\Delta \hat{G}^\circ_{\mathrm{rxn}}$ is the standard-state Gibbs free energy of reaction, R is the ideal gas constant, T is the temperature, P is pressure at the AMOI, and P° is the standard-state pressure (1 bar in this case). The index i spans all species, while g refers to gas-phase species only, for which we include a pressure dependence.

In addition to the equilibrium conditions, we add three equations enforcing mass balance constraints by requiring that the mole fractions in each phase sum to unity:

$$1 - \sum_i x_{i,k} = 0, \tag{3}$$

where $x_{i,k}$ is the mole fraction of component i in phase k.

We impose elemental conservation by introducing seven additional sum constraints—one for each conserved element:

$$n_s - \sum_i \sum_k n_{s,i,k} x_{i,k} N_k = 0, \tag{4}$$

where n_s is the total number of moles of element s, $x_{i,k}$ is the mole fraction of component i in phase k, $n_{s,i,k}$ is the number of atoms of element s in component i of phase k, and N_k is the total number of moles of phase k. In our model, both the mole fractions $x_{i,k}$ and the total moles for phases k = metal, silicate, or gas, N_k, are treated as variables. The pressure at the AMOI is implied by the derived mean molecular weight of the atmosphere.

We solve for the global chemical equilibrium following the numerical scheme of H. E. Schlichting & E. D. Young (2022), but with key adaptations that reduce the computational time from approximately 30 minutes to a few tens of seconds on a single CPU. The details of these improvements are presented in S. L. Grimm et al. (2025, in preparation).

2.2. Thermodynamic Data

To solve the chemical equilibrium network, we require the standard-state molar Gibbs free energies of reaction, $\Delta\hat{G}^{\circ}_{\rm rxn}$. These values are calculated following the approach described in H. E. Schlichting & E. D. Young (2022). Where available, we use internally consistent Gibbs free energies of formation for silicate and metal species. Ideal mixing is assumed for all phases except for Si and O in metal (E. D. Young et al. 2023). When direct thermodynamic data are not available for a given species, we derive its Gibbs free energy of formation by combining the free energies of known species with known free energies of reaction.

Following H. E. Schlichting & E. D. Young (2022), we do not apply pressure corrections to the Gibbs free energies of silicate species. This choice is motivated by the expectation that pressure effects for intramelt reactions are minor and may largely cancel out (see L. Stixrude & B. Karki 2005; N. De Koker & L. Stixrude 2009; H. E. Schlichting & E. D. Young 2022). Nonetheless, additional thermodynamic constraints are needed to more robustly assess these effects. Similarly, no pressure corrections are applied to metal species. For the detailed derivation of the thermodynamic data and reaction framework, we refer the reader to the appendix in H. E. Schlichting & E. D. Young (2022).

2.3. Siderophile Behavior of Carbon

We rely on experimentally determined partitioning of carbon between metal and silicate phases in order to evaluate the free energy of Reaction (1). We assume that the concentration of carbon in the silicate, expressed as $x_{CO,silicate}$, is equivalent to $x_{C,silicate}$ in the experiments. Experimental measurements of carbon partitioning vary significantly, particularly in their pressure dependence, which is of key importance in the present context. D. S. Grewal et al. (2019) report an increase in the siderophile (iron-loving) behavior of carbon with increasing pressure, whereas R. A. Fischer et al. (2020) find the opposite trend.

For this study, we adopt the carbon partitioning behavior from I. Blanchard et al. (2022), who used ^{13}C to avoid potential contamination from the diamond anvil cell. In addition, I. Blanchard et al. (2022) excluded large quenched metal blebs from their silicate analyses, which may not reliably reflect high-pressure equilibrium conditions. In contrast, R. A. Fischer et al. (2020) included such blebs, interpreting them as quench artifacts and assuming they would have been dissolved at high pressure and temperature. I. Blanchard et al. (2022) also noted that they were not able to reproduce the high partitioning fits reported by D. S. Grewal et al. (2019). For these reasons, we adopt the partitioning data from I. Blanchard et al. (2022). In our model, this yields carbon partitioning behavior intermediate between that of R. A. Fischer et al. (2020) and that of D. S. Grewal et al. (2019).

In order to assess the role of carbon partitioning to the metal phase, we run the entire planetary grid both with the full chemical network described in Section 2.1 and with the original reaction network from H. E. Schlichting & E. D. Young (2022), which excludes both Reaction (1) and carbon in the metal phase. This comparison allows us to isolate and quantify the effect of carbon in the metal phase on the atmospheric C/O ratio.

2.4. Linking Deep Atmosphere with Observable Upper Atmosphere

To assess how the chemical composition of the deep atmosphere, as set by equilibrium with the magma ocean, is transmitted to the observable upper layers of the atmosphere, we employ a suite of open source atmospheric models: `FastChem` (J. W. Stock et al. 2018), `HELIOS` (M. Malik et al. 2017, 2019), `VULCAN` (S.-M. Tsai et al. 2017), and `HELIOS-K` (S. L. Grimm et al. 2021). These models together enable the simulation of chemical equilibrium, photochemistry, and radiative transfer with species-dependent opacities over a broad pressure range.

`FastChem` computes gas-phase chemical equilibrium under local thermodynamic conditions. `HELIOS` is a 1D radiative-convective model used to compute pressure–temperature (*P-T*) profiles. `HELIOS-K` calculates wavelength-dependent opacities for given gas mixtures. `VULCAN` is a solver for kinetic reaction networks that incorporates thermochemistry, photochemistry, vertical mixing, and condensation. Together, these models allow us to simulate atmospheric structures from the magma ocean interface to atmospheric pressures of 10^{-8} bar.

Using these codes, our workflow is as follows. We first calculate the atmospheric composition above the magma obtained using our global equilibrium model. We then use `FastChem` to define the molar equilibrium mixing ratios of gas species for this composition for a *P-T* grid representing possible atmospheric conditions above the magma ocean. This output is passed to `HELIOS-K` to compute gas opacities, which in turn serve as inputs for `HELIOS` to derive the atmosphere *P-T* profile. The *P-T* profile, along with the gas composition above the magma ocean, comprising the lower boundary condition, is fed into `VULCAN` to compute the steady-state chemical structure. We use the output from `VULCAN` to recompute the opacities with `HELIOS-K` and update the *P-T* structure with `HELIOS`. This iterative cycle between `HELIOS`/`HELIOS-K` and `VULCAN` is repeated until convergence is achieved in both the mixing ratios and the *P-T* profile. The pressure grid in `HELIOS` extends from the AMOI pressure up to 10^{-5} bar. In `VULCAN`, we assume perfect mixing in the deep convective layer and begin calculating chemical kinetics from 10^{3} bar to high altitudes. The atmospheric structure modeling is of high computational cost (a few hours), and therefore we restrict this analysis to a representative case rather than a full grid.

2.5. Simulation Setup

The initial planetary compositions used in this study follow the model of E. D. Young et al. (2023), with the addition of

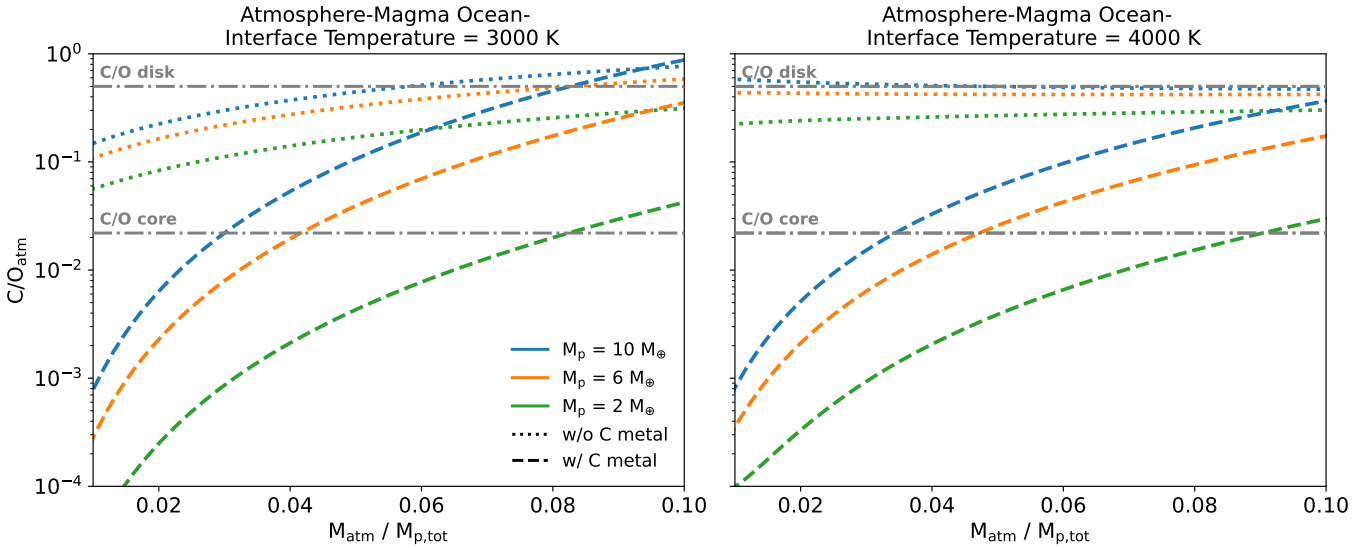

Figure 1. Molar bulk atmospheric C/O ratio as a function of atmospheric mass fraction. Dashed lines show results from the reaction network that includes carbon in the metal phase; dotted lines show results from the network excluding carbon in the metal phase. The horizontal dashed lines indicate the initial C/O ratios of the disk and the core. The core C/O ratio is calculated from the initial conditions for the case with C metal. The left panel shows models with an atmosphere–magma ocean interface (AMOI) temperature of 3000 K and a silicate–metal equilibrium (SME) temperature of 3500 K. The right panel shows models with an AMOI temperature of 4000 K and an SME temperature of 4500 K. Including carbon in the metal phase leads to a decrease in the atmospheric C/O ratio at low atmospheric mass fractions.

carbon in the metal phase. All C/O ratios reported in this study are given in mole units. The silicate phase of the core is composed of 94.7% (molar) $MgSiO_3$, 3.3% MgO, 1.1% SiO_2, 0.7% Na_2O, 0.1% Na_2SiO_3, and minor amounts of FeO and $FeSiO_3$. The initial envelope is hydrogen-dominated, consisting of 99.9% H_2 and 0.1% CO_2 by mole, corresponding to a solar C/O ratio of 0.5 (by moles; L. Suárez-Andrés et al. 2018). The initial metal phase of the core is Fe-rich. In the models where we include C metal, we add 6.5% (molar) C to the initial metal phase, corresponding to an initial core composition of 0.5 wt% carbon and a C/O ratio of 0.02. This is different in the case when no reactive carbon in the metal is assumed, which implies nearly zero weight percent carbon available for reaction in the cores and commensurately small core C/O ratio of near zero. In those models where we exclude C metal, the initial metal phase available for reaction is assumed to be 99.9% Fe by mole. In both setups, trace amounts of H and Si are also included in the metal phase. We choose these two scenarios as a means of isolating the role that carbon in metal has on the results, rather than the bulk carbon concentration of the core (i.e., there can be carbon sequestered in metal that is not reactive).

The total planetary mass ranges from 2 to 10 $M_\oplus$, and we explore atmospheric mass fractions from 0.1% to 10%. For each configuration, we consider two thermal states: one with an AMOI temperature of 3000 K and an SME temperature of 3500 K, and another with an AMOI temperature of 4000 K and an SME temperature of 4500 K. The greater SME temperature is meant to simulate silicate–metal equilibration within the magma ocean but at modest depths, as expected for these underdense metals.

3. Results

3.1. C/O Ratio as a Function of Atmospheric Mass Fraction and Planetary Mass

Figure 1 shows the bulk atmospheric C/O ratio as a function of atmospheric mass fraction for planets with 2, 6, and 10 $M_\oplus$ and AMOI temperatures of 3000 and 4000 K. The corresponding SME temperatures are 3500 and 4500 K, respectively. Colored dashed lines represent simulations that include carbon in the metal phase, allowing carbon to partition into the metal via Reaction (1). Colored dotted lines show results from simulations where carbon is excluded from the metal phase. The core (including silicates and metals) and disk C/O ratios are shown as horizontal gray dashed lines. The core C/O ratio is calculated from the initial conditions used in simulations, with 0.5 wt% carbon in the core for the case with metal C, and zero in the C metal-free case. Therefore, the initial C/O for the core shown in Figure 1 applies only to the cases with metal carbon included.

In models that include carbon in the metal phase, the atmospheric C/O ratio decreases sharply at low atmospheric mass fractions, deviating by several orders of magnitude from the disk value. This effect is strongest for low-mass planets with small atmospheric mass fractions. At high atmospheric mass fractions, the C/O ratio approaches the initial disk value, as less carbon is sequestered into the core relative to the available volatile reservoir.

In contrast, models that exclude carbon in the metal phase yield significantly higher atmospheric C/O ratios, which remain nearly constant across all atmospheric mass fractions, particularly at the higher AMOI temperature of 4000 K. This behavior occurs because a higher SME temperature increases oxygen partitioning into the metal phase, leading to a depletion of oxygen in the atmosphere. Since a sink for carbon is absent, the amount of carbon in the atmosphere remains nearly constant. This combination results in an elevated and nearly constant C/O ratio.

The exact atmospheric C/O ratio depends on both the SME temperature and the adopted carbon partitioning fit. In particular, we find that increasing the SME temperature from 3500 to 4000 K (for an AMOI temperature of 3000 K) can increase the atmospheric C/O ratio by up to 2 orders of magnitude for a given envelope mass fraction. However, the results are less sensitive to the choice of carbon partitioning fit:

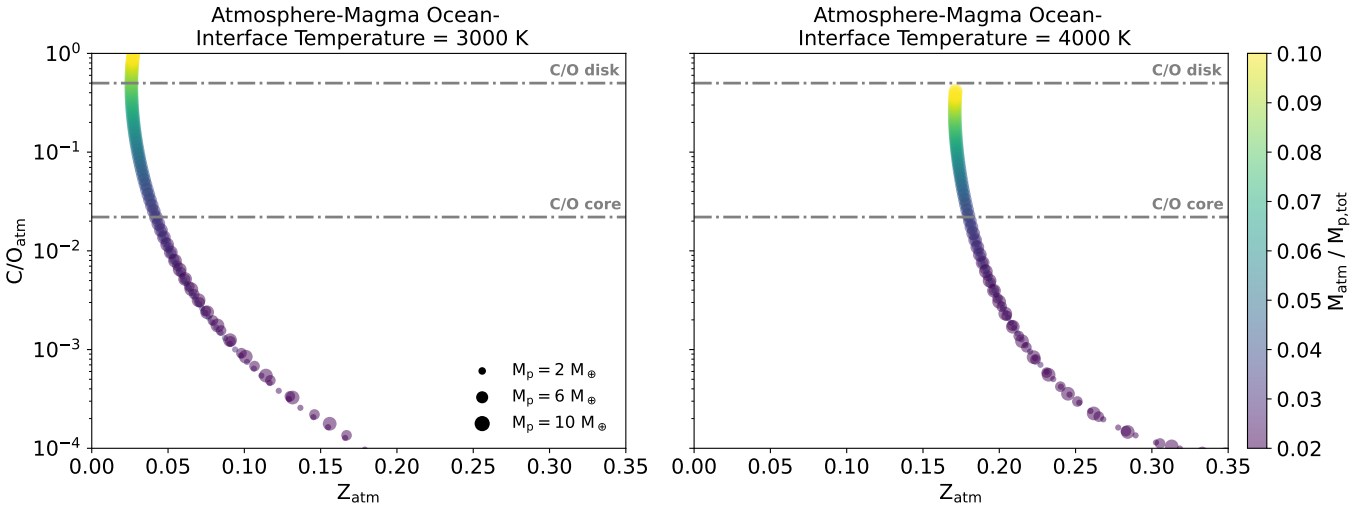

Figure 2. Molar bulk atmospheric C/O ratio as a function of resulting atmospheric metal mass fraction, Z_{atm}, for all models that include carbon in the metallic phase (from Figure 1). Horizontal dashed lines mark the initial C/O ratios of the disk and the core. The color bar indicates atmospheric mass fraction. Z_{atm} is defined as the mass fraction of all atmospheric constituents except hydrogen, divided by the total atmospheric mass. Circle sizes denote different planetary masses. The left panel shows models with an atmosphere–magma ocean interface (AMOI) temperature of 3000 K and a silicate–metal equilibrium (SME) temperature of 3500 K; the right panel shows models with AMOI temperature of 4000 K and SME temperature of 4500 K. Across all cases, the atmospheric C/O ratio decreases with increasing Z_{atm}, independently of planetary mass.

using the 1σ uncertainty fit from I. Blanchard et al. (2022) leads to only minor deviations in the resulting C/O ratios. While the absolute values depend on these parameters, the overall trends with planetary mass and atmospheric mass fraction remain robust. Figures illustrating the sensitivity analysis are provided in the Appendix.

3.2. C/O Ratio as a Function of Atmospheric Metal Mass Fraction

Figure 2 shows the bulk atmospheric C/O ratio as a function of the atmospheric metal mass fraction, Z_{atm}, where all atoms other than hydrogen are considered metals (our models do not include He). Horizontal dashed lines indicate the initial disk and core C/O ratios. Only models that include carbon in the metal phase are shown. Each data point corresponds to an individual planet from Figure 1. The left and right panels represent AMOI temperatures of 3000 and 4000 K, respectively. Circle size denotes planetary mass, and the color bar indicates atmospheric mass fraction. Across all planetary masses and atmospheric mass fractions, the data collapse onto temperature-dependent sequences. At higher AMOI temperatures, enhanced evaporation of species like Mg, Si, Fe, and especially SiO leads to higher atmospheric metallicities and atmospheric mass fractions at a given C/O ratio. The increased abundance of SiO lowers the atmospheric C/O ratio, thereby shifting the entire distribution toward higher Z_{atm} and lower C/O.

In addition to that, the atmospheric C/O ratio decreases with increasing Z_{atm}. This trend can best be understood by examining Figure 3, which shows the bulk atmospheric mixing ratios of the dominant carbon- and oxygen-bearing species as a function of atmospheric C/O ratio for the 3000 K case with carbon in the metallic phase. Horizontal dashed lines indicate the initial C/O ratios of the disk and the core. As the bulk atmospheric C/O ratio increases—corresponding to planets with higher masses, higher atmospheric mass fractions, and thus higher AMOI pressures—CH_4 becomes more abundant while H_2O decreases. These changes in molecular abundances

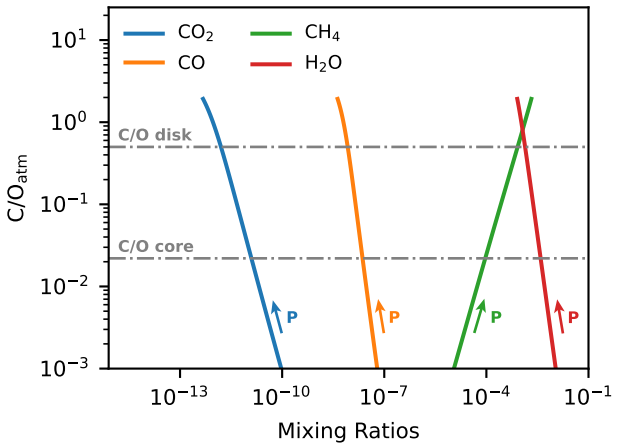

Figure 3. Molar bulk atmospheric C/O ratio as a function of species mixing ratios for the 3000 K atmosphere–magma ocean interface (AMOI) temperature models with carbon in the metallic phase, from Figure 1. Horizontal dashed lines indicate the initial C/O ratios of the disk and the core. *P* denotes AMOI pressure, which increases with increasing atmospheric C/O ratio. At high atmospheric mass fractions and planetary masses—corresponding to higher pressures—the atmosphere is carbon-rich and CH_4-dominated, driving up the C/O ratio. At low atmospheric mass fractions and low pressures, H_2O becomes more abundant, and the C/O ratio decreases.

explain the trend in atmospheric metal mass fraction seen in Figure 2: at low Z_{atm} (high atmospheric mass fractions), the atmosphere is carbon-rich and CH_4-dominated, driving up the C/O ratio. At higher Z_{atm} (low atmospheric mass fractions), H_2O becomes dominant, lowering the C/O ratio. Overall, the atmospheric C/O ratio increases with atmospheric mass fraction and planetary mass (see Figure 1), and thus with AMOI pressure *P*.

3.3. Vertical Transport and the Observability of the C/O Ratio

Figure 4 shows the atmospheric structure of a $6\,M_\oplus$ planet selected from the 3000 K AMOI temperature case shown in Figure 1. We assume a radius of $2.5\,R_\oplus$, defined at 1 bar atmospheric pressure. The equilibrium temperature is

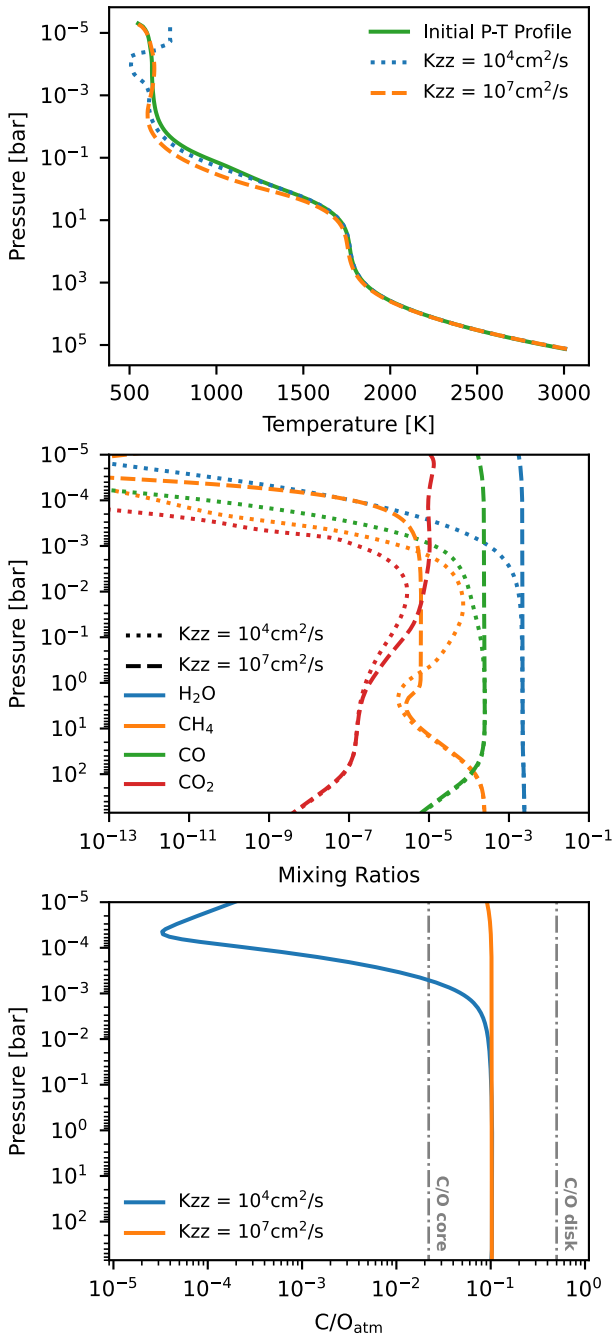

Figure 4. Atmospheric structure for a $6\,M_\oplus$ and $2.5\,R_\oplus$ planet with an atmosphere–magma ocean interface temperature of 3000 K and an equilibrium temperature of ≈600 K. The radius is defined at 1 bar atmospheric pressure. All panels show results for two different eddy diffusion coefficients, $K_{zz} = 10^4$ and 10^7 $\mathrm{cm^2 s^{-1}}$, which control vertical mixing in the atmosphere. The stellar spectrum is modeled as a blackbody. The top panel shows the pressure–temperature profile before and after convergence; the middle panel shows the vertical variations in mixing ratios of the dominant carbon- and oxygen-bearing species; and the bottom panel shows the molar atmospheric C/O ratio as a function of pressure. Dashed vertical lines in the bottom panel indicate the initial C/O ratios of the disk and the core, highlighting the distinct C/O ratios of the atmosphere compared to the core and disk. Lower vertical mixing rates lead to stronger vertical gradients in the atmospheric C/O ratio.

approximately 600 K, corresponding to an orbital distance of 0.1 au around a 5200 K star. The stellar spectrum is modeled as a blackbody. We consider two vertical mixing scenarios with eddy diffusion coefficients of $K_{zz} = 10^4$ and 10^7 $\mathrm{cm^2\,s^{-1}}$. The top panel shows the *P-T* profile before and after convergence. The middle panel presents vertical variation in mixing ratios of the dominant oxygen- and carbon-bearing species from 10^3 to 10^{-5} bar. In the low-mixing case, these mixing ratios drop significantly above $\sim 10^{-2}$ bar, while they remain approximately constant (except for CH_4) in the high-mixing case. The bottom panel displays the atmospheric C/O ratio calculated from all carbon and oxygen-bearing species. Vertical dashed gray lines indicate the initial C/O ratios of the disk and the core. In the high-mixing scenario, the C/O ratio remains constant with altitude, whereas in the low-mixing case it decreases above $\sim 10^{-2}$ bar.

We calculate the molar C/O ratio using all carbon- and oxygen-bearing species output by VULCAN. In the low-mixing case, the observed drop in C/O ratio above $\sim 10^{-2}$ bar is primarily driven by gravitational settling. At these low pressures, heavier species with smaller scale heights—such as CO_2 (44 u) and CO (28 u)—settle more efficiently than lighter species like CH_4 (16 u) and H_2O (18 u; S.-M. Tsai et al. 2021). In our simulations, H_2O remains the dominant oxygen-bearing species throughout the envelope. As CH_4 overtakes CO as the main carbon carrier, the C/O ratio rises slightly at high altitudes.

Photochemistry also contributes to the depletion of CO, CH_4, and H_2O at low pressures, but its impact on the C/O ratio is secondary, as the abundances of photochemical products remain minor in our simulations. In general, the downward transport and eventual destruction of photochemical products may aid in removing some carbon and oxygen from the upper atmosphere (S.-M. Tsai et al. 2021), but the effect on the C/O ratio is negligible.

In contrast, in the high-mixing case, efficient vertical transport continuously mixes carbon- and oxygen-bearing species throughout the atmosphere, preventing their depletion and maintaining a constant C/O ratio with altitude.

Typical observable regions in planetary atmospheres span pressure ranges of 10^{-1}–10^{-3} bar for emission spectroscopy (A. A. A. Piette et al. 2023) and 10^{-3}–10^{-5} bar for transmission spectroscopy (B. Benneke et al. 2024). Both vertical mixing scenarios yield the same observable C/O ratio in emission, but in transmission spectroscopy the C/O ratio is affected by vertical mixing: in the low-mixing case, the C/O ratio decreases across observable pressures, while it remains constant in the high-mixing scenario.

4. Discussion

We find that the atmospheric C/O ratio in sub-Neptunes is not inherited from the protoplanetary disk, but instead emerges from chemical equilibrium between the atmosphere and the underlying magma ocean. In itself, this result should not be surprising, since most of the mass (>90%) of sub-Neptunes investigated here resides in their magma-ocean and metal interiors. These interiors can therefore significantly modify the C/O ratio of the primordial hydrogen envelope that typically only contains a couple of percent of the total planet's mass. Specifically, we find that the C/O ratio increases with planetary mass and atmospheric mass fraction, yet remains distinct from both disk and core values. Including carbon in the metal phase reduces the atmospheric C/O ratio significantly, particularly for planets with low masses and low atmosphere mass fractions. The finding is particularly exciting, since it implies that observed C/O ratios of sub-Neptunes can be used to probe their interior composition and chemistry. Specifically,

the detection of C/O ratios that are much lower than host star values would imply an underlying magma ocean with iron metal having sequestered a lot of the carbon.

Recent studies suggest that SiH_4 may be an important tracer of magma ocean activity (S. Charnoz et al. 2023; W. Misener et al. 2023) and could be detectable even at low pressures (Y. Ito et al. 2025). Although SiH_4 was not included in our main simulations, we conducted preliminary tests by adding it to the chemical network to explore its potential impact. These tests indicate that SiH_4 reduces the atmosphere and significantly promotes CH_4 formation, leading to elevated C/O ratios. However, since CH_4 is rapidly depleted within the envelope, high near-surface CH_4 abundances may not translate into elevated C/O ratios in observable regions. Exploring the full implications of SiH_4 is beyond the scope of this study but represents an important direction for future work.

Questions regarding magma ocean–atmosphere interactions have been explored by M. Tian & K. Heng (2024) and C. Seo et al. (2024), who model their influence on atmospheric composition without accounting for metal-silicate partitioning. M. Tian & K. Heng (2024) explore a C–H–O system using imposed redox parameters and initial atmospheric compositions, and find that the atmospheric C/O ratio decreases with pressure. Their models predict CO and CO_2 as the dominant carbon-bearing species across a wide range of conditions, with CH_4 never emerging as the major component. In contrast, our chemical equilibrium model consistently yields CH_4 as the dominant carbon carrier in the deep atmosphere and an increasing C/O ratio with pressure. While M. Tian & K. Heng (2024) do not include photochemistry, we explicitly couple our interior compositions to 1D atmospheric models that incorporate vertical mixing and photochemical kinetics. For the atmosphere structure we analyzed, CH_4 is efficiently destroyed above $\sim 10^{-2}$ bar (low K_{zz}) and $\sim 10^{-3}$ bar (high K_{zz}), leading to a transition where CO and CO_2 become the dominant carbon-bearing species in the observable atmosphere. This transition is in agreement with the results of M. Tian & K. Heng (2024), though in our case it arises from photochemical depletion of CH_4 rather than equilibrium chemistry alone. In addition, M. Tian & K. Heng (2024) also analyzes an extended C–H–O–N–S network, which lies outside the scope of direct comparison due to the absence of sulfur and nitrogen in our model.

C. Seo et al. (2024) similarly study magma–gas equilibrium under various planetary conditions and find that O/H decreases with increasing C/O, a trend we also reproduce. While M. Tian & K. Heng (2024) investigate AMOI temperatures between 1600 and 1800 K, C. Seo et al. (2024) explore atmospheric compositions up to 4000 K and derive the redox state of the mantle self-consistently from the assumed bulk composition.

Our work differs from both studies in two key aspects. First, we include a metal phase and allow carbon to partition into it, introducing a major sink that strongly modulates atmospheric composition. Second, we include a reaction between the metal and silicate phases that produces H_2O, providing an internal oxygen source that significantly influences the atmospheric C/O ratio.

Finally, we note that CH_4 is not included as a silicate species in our simulations, so direct dissolution into the melt is not explicitly accounted for. Given the low solubilities of CH_4 in silicate melts (P. Ardia et al. 2013), inclusion of an explicit reaction for CH_4 dissolution is unlikely to have an impact on our results.

5. Conclusion

Our results demonstrate that atmospheric C/O ratios in sub-Neptunes are not inherited from the protoplanetary disk if there is a magma ocean beneath the dense H_2-rich atmosphere. Under these circumstances, the atmospheric C/O ratio cannot be used directly as a tracer of planet formation location or disk chemistry, as is often assumed for hot Jupiters and some small icy solar system bodies. Instead, the C/O ratio is significantly modified by chemical equilibrium between the atmosphere and the underlying magma ocean. We show that partitioning of carbon to the metallic phase further reduces the atmospheric C/O ratio, especially for low-mass planets with low atmosphere mass fractions. This internal processing decouples the atmospheric composition from its primordial origin. Importantly, we find that the deep C/O ratio is largely preserved in the observable atmosphere, opening up the opportunity to probe the interior composition and chemistry using spectroscopic observations of sub-Neptunes. For example, the detection of C/O ratios that are much lower than host star values would imply an underlying magma ocean with iron metal having sequestered a lot of the carbon.

These results suggest that atmospheric retrievals assuming disk-based C/O priors may lead to biased results.

Our findings provide a framework in which to interpret the observed compositional diversity in sub-Neptunes and motivate future work exploring additional chemical species, time-dependent evolution, and application to JWST targets.

Acknowledgments

C.D. acknowledges support from the Swiss National Science Foundation under grant TMSGI2_211313. H.E.S. gratefully acknowledges support from NASA under grant No. 80NSSC18K0828. E.D.Y. acknowledges support from NASA grant No. 80NSSC21K0477 issued through the Emerging Worlds program. This work has been carried out within the framework of the NCCR PlanetS supported by the Swiss National Science Foundation under grant 51NF40_205606. We thank the anonymous reviewer for insightful comments, which greatly helped to improve this study. We acknowledge the use of large language models (LLMs), including ChatGPT, to improve the grammar, clarity, and readability of the manuscript.

Appendix
Model Sensitivity Tests

To assess the sensitivity of our model to key assumptions, we reran the atmospheric C/O ratio calculations for a $6\,M_\oplus$ planet with varying atmospheric mass fraction, as in Figure 1. In Figure 5, we explore the impact of different carbon partitioning fits, using alternative fits from I. Blanchard et al. (2022) that span the 1σ uncertainty range. In Figure 6, we test the effect of increasing the SME temperature from 500 to 1000 K above the AMOI temperature.

We find that the partitioning fit only moderately shifts the absolute C/O ratio. In contrast, the SME temperature has a significant effect, changing the atmospheric C/O ratio by up to 2 orders of magnitude. This strong sensitivity arises because higher SME temperatures increase the oxygen partitioning into the metal phase, reducing the oxygen available in the

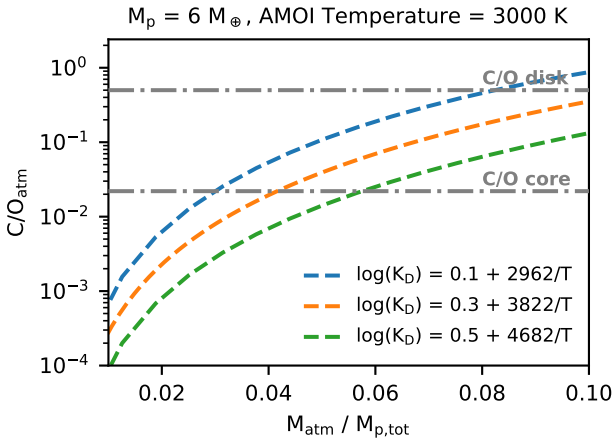

Figure 5. Molar bulk atmospheric C/O ratio as a function of atmospheric mass fraction. A 6 $M_\oplus$ planet with an atmosphere–magma ocean interface (AMOI) temperature of 3000 K and a silicate–metal equilibrium (SME) temperature of 3500 K is shown. The orange dashed line reproduces the default case from Figure 1. Two additional curves illustrate the effect of different carbon partitioning fits from I. Blanchard et al. (2022), spanning the 1σ uncertainty range. Horizontal dashed lines indicate the initial C/O ratios of the disk and the core, with the core value derived from the initial conditions in the C-metal case.

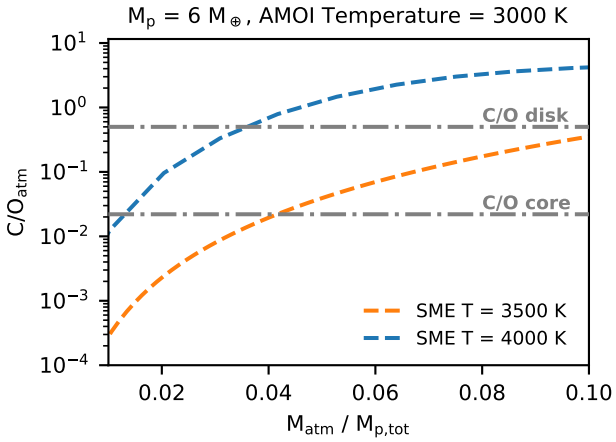

Figure 6. Same as Figure 5, but showing the effect of varying the silicate–metal equilibrium (SME) temperature. Both curves use the same carbon partitioning fit as in Figure 1. The orange curve corresponds to the default case from Figures 1 and 5, while the blue curve corresponds to an SME temperature of 4000 K. Increasing the SME temperature leads to significantly higher C/O ratios due to enhanced oxygen partitioning into the metal phase.

atmosphere. Despite these variations in absolute values, the qualitative trends and overall conclusions remain robust.

ORCID iDs

Aaron Werlen https://orcid.org/0009-0005-1133-7586
Caroline Dorn https://orcid.org/0000-0001-6110-4610
Hilke E. Schlichting https://orcid.org/0000-0002-0298-8089
Simon L. Grimm https://orcid.org/0000-0002-0632-4407
Edward D. Young https://orcid.org/0000-0002-1299-0801

References

Ardia, P., Hirschmann, M. M., Withers, A. C., & Stanley, B. D. 2013, GeCoA, 114, 52
Benneke, B., Roy, P.-A., Coulombe, L.-P., et al. 2024, arXiv:2403.03325
Blanchard, I., Rubie, D. C., Jennings, E. S., et al. 2022, E&PSL, 580, 117374
Chachan, Y., & Stevenson, D. J. 2018, ApJ, 854, 21
Charnoz, S., Falco, A., Tremblin, P., et al. 2023, A&A, 674, A224
Crossfield, I. J. M., Barman, T., Hansen, B. M. S., Tanaka, I., & Kodama, T. 2012, ApJ, 760, 140
De Koker, N., & Stixrude, L. 2009, GeoJI, 178, 162
Felix, L., Kitzmann, D., Demory, B.-O., & Mordasini, C. 2025, arXiv:2504.13039
Fischer, R. A., Cottrell, E., Hauri, E., Lee, K. K. M., & Le Voyer, M. 2020, PNAS, 117, 8743
Ginzburg, S., Schlichting, H. E., & Sari, R. 2016, ApJ, 825, 29
Grewal, D. S., Dasgupta, R., Sun, C., Tsuno, K., & Costin, G. 2019, SciA, 5, eaau3669
Grimm, S. L., Malik, M., Kitzmann, D., et al. 2021, ApJS, 253, 30
Helling, C., Woitke, P., Rimmer, P. B., et al. 2014, Life, 4, 142
Hirao, N., Kondo, T., Ohtani, E., Takemura, K., & Kikegawa, T. 2004, GeoRL, 31
Holmberg, M., & Madhusudhan, N. 2024, A&A, 683, L2
Ito, Y., Kimura, T., Ohno, K., Fujii, Y., & Ikoma, M. 2025, ApJ, 987, 174
Kite, E. S., Fegley, B., Jr., Schaefer, L., & Ford, E. B. 2019, ApJL, 887, L33
Kite, E. S., & Schaefer, L. 2021, ApJL, 909, L22
Kreidberg, L., Line, M. R., Bean, J. L., et al. 2015, ApJ, 814, 66
Lee, E. J., & Chiang, E. 2015, ApJ, 811, 41
Li, Y., Vočadlo, L., Sun, T., & Brodholt, J. P. 2020, NatGe, 13, 453
Line, M. R., Knutson, H., Wolf, A. S., & Yung, Y. L. 2014, ApJ, 783, 70
Lopez, E. D., & Fortney, J. J. 2014, ApJ, 792, 1
Madhusudhan, N., Amin, M. A., & Kennedy, G. M. 2014, ApJL, 794, L12
Madhusudhan, N., Harrington, J., Stevenson, K. B., et al. 2011, Natur, 469, 64
Madhusudhan, N., Sarkar, S., Constantinou, S., et al. 2023, ApJL, 956, L13
Malik, M., Grosheintz, L., Mendonça, J. M., et al. 2017, AJ, 153, 56
Malik, M., Kitzmann, D., Mendonça, J. M., et al. 2019, AJ, 157, 170
Marboeuf, U., Thiabaud, A., Alibert, Y., Cabral, N., & Benz, W. 2014a, A&A, 570, A36
Marboeuf, U., Thiabaud, A., Alibert, Y., Cabral, N., & Benz, W. 2014b, A&A, 570, A35
Misener, W., Schlichting, H. E., & Young, E. D. 2023, MNRAS, 524, 981
Mordasini, C., van Boekel, R., Mollière, P., Henning, T., & Benneke, B. 2016, ApJ, 832, 41
Mousis, O., Marboeuf, U., Lunine, J. I., et al. 2009, ApJ, 696, 1348
Mousis, O., Werlen, A., Benest Couzinou, T., & Schneeberger, A. 2025, ApJL, 983, L12
Öberg, K. I., Murray-Clay, R., & Bergin, E. A. 2011, ApJL, 743, L16
Piette, A. A. A., Gao, P., Brugman, K., et al. 2023, ApJ, 954, 29
Schlichting, H. E., & Young, E. D. 2022, PSJ, 3, 127
Schmidt, S. P., MacDonald, R. J., Tsai, S.-M., et al. 2025, arXiv:2501.18477
Seo, C., Ito, Y., & Fujii, Y. 2024, ApJ, 975, 14
Stixrude, L., & Karki, B. 2005, Sci, 310, 297
Stock, J. W., Kitzmann, D., Patzer, A. B. C., & Sedlmayr, E. 2018, MNRAS, 479, 865
Suárez-Andrés, L., Israelian, G., Hernández, J. I. G., et al. 2018, A&A, 614, A84
Swain, M., Deroo, P., Tinetti, G., et al. 2013, Icar, 225, 432
Tagawa, S., Sakamoto, N., Hirose, K., et al. 2021, NatCo, 12, 2588
Terasaki, H., Ohtani, E., Sakai, T., et al. 2009, GeCAS, 73, A1321
Thiabaud, A., Marboeuf, U., Alibert, Y., Leya, I., & Mezger, K. 2015, A&A, 574, A138
Thiabaud, A., Marboeuf, U., Alibert, Y., et al. 2014, A&A, 562, A27
Tian, M., & Heng, K. 2024, ApJ, 963, 157
Tsai, S.-M., Lyons, J. R., Grosheintz, L., et al. 2017, ApJS, 228, 20
Tsai, S.-M., Malik, M., Kitzmann, D., et al. 2021, ApJ, 923, 264
Young, E. D., Shahar, A., & Schlichting, H. E. 2023, Natur, 616, 306
Young, E. D., Stixrude, L., Rogers, J. G., Schlichting, H. E., & Marcum, S. P. 2024, PSJ, 5, 268